MDPI

Article

Physical and Numerical Experimentation of Water Droplet Collision on a Wall: A Comparison between PLIC and HRIC Schemes for the VOF Transport Equation with High-Speed Imaging

Bruno Silva de Lima [1,*,†] , Martin Sommerfeld [2,†] and Francisco José de Souza [1,†]

1   School of Mechanical Engineering, Federal University of Uberlândia, João Naves de Ávila Avenue, 2121, Bloco 5P, Uberlândia 38400-902, Brazil; francisco.souza@ufu.br
2   Faculty of Process and Systems Engineering, Otto von Güricke Universität Magdeburg, Hoher Weg 7, 06120 Halle (Saale), Germany; martin.sommerfeld@ovgu.de
*   Correspondence: brunosilvadelima@hotmail.com
†   These authors contributed equally to this work.

Abstract: Liquid films are often found in engineering applications with thicknesses ranging from micrometer scales to large scales with a wide range of applications. To optimize such systems, researchers have dedicated themselves to the development of new techniques. To further contribute to this development, the objective of this work is to present the results of the collision of water droplets on a wall by means of experimentation and numerical simulations. For physical experimentation, an injector is used to generate a chain of water droplets that collide with the opposite wall, forming a liquid film. Images of the droplets were obtained using two high-speed recording cameras. The results for different droplet sizes and impact angles are presented and the relationship between the momentum parameter and non-dimensional pool size was established. Modeling such processes is a common challenge in engineering, with different techniques having their advantages and limitations. The simulations in this work were run using the volume of fluid method, which consists of solving a transport equation for the volume fraction of each considered fluid. A correlation was found between the surface tension to momentum transport ratio, Scd, and the non-dimensional pool size for different droplet sizes and impact angles. Regions where partial depositions were most likely to occur were found via physical experiments.

Keywords: volume of fluid; droplet collision; HRIC; PLIC; droplet wall interaction

1. Introduction

The study of droplet collisions holds significant importance in engineering, given its widespread presence across various applications. Among these applications, industrial processes such as painting, irrigation, coating, and fuel injection stand out. Proper characterization and application of instruments are imperative for optimizing the performance of these systems. For instance, consider the fuel spray inside a combustion chamber, which, if properly applied, can lead to the formation of a liquid film on the chamber walls. Such a film not only decreases combustion efficiency but also serves as a source of soot particles and unburned hydrocarbons, directly impacting fuel economy and contributing to increased pollutants [1–3]. Similarly, in coating processes, correct equipment usage not only conserves materials and time but also enhances surface finishing, eliminating the need for additional processes [4,5].

Understanding the underlying physics is crucial for controlling and enhancing these processes [6]. Both physical experiments and numerical simulations, employing diverse technologies, play pivotal roles in unraveling complex engineering challenges.

Researchers are actively engaged in refining descriptions of droplet collision phenomena and liquid film formation. For example, Diez et al. [7] devised an analytical solution using lubrication theory to study the spread of viscous droplets on smooth horizontal surfaces. Their findings, validated against experimental data, underscore the time-independence of results and their significance in model validation.

Accurate simulation of fluid interactions presents a major challenge. Various methodologies, including front-tracking, level-set, and VOF methods, are employed to track fluid interfaces [8]. The level-set approach, although effective in capturing topological changes, lacks mass conservation, unlike the VOF method, which ensures local and global mass conservation [9].

The level-set method, for instance, tracks the evolution of an interface implicitly by propagating a signed distance function. While effective in capturing topological changes with high fidelity, it falls short in preserving mass conservation, a critical aspect in many engineering applications [9]. On the other hand, the VOF method, which solves a scalar transport equation for volume fractions, ensures both local and global mass conservation, albeit at the cost of computational complexity [9].

Within the realm of VOF simulations, the challenge lies in accurately reconstructing fluid interfaces from discrete volume fractions. Geometric schemes like PLIC (piecewise-linear interface calculation) and algebraic schemes such as HRIC (high-resolution interface capturing) offer contrasting approaches to this dilemma, each with its own set of advantages and limitations [6].

Research endeavors further delve into specific phenomena, such as flow patterns generated by impingement on a wall [10], erosion caused by droplet impact [11], and the dynamics of rising bubbles [9]. These investigations, conducted via numerical simulations and physical experiments, provide insights into factors influencing outcomes, such as viscosity, droplet properties, and environmental conditions.

In parallel, advancements in numerical modeling hold promise for enhanced predictive capabilities. Innovations such as the incorporation of adhesion forces and interface sharpening schemes not only refine simulation accuracy but also pave the way for a deeper understanding of interfacial phenomena [12,13].

High-speed imaging techniques, coupled with computational simulations, offer a synergistic approach to unraveling complex fluid dynamics. By providing visual insights into transient phenomena, such as droplet spreading and breakup, these techniques complement numerical simulations and aid in model validation [14].

Yet, amid these advancements, challenges persist. Comparative studies, such as the evaluation of interpolation schemes for density interpolation, underscore the need for robust numerical methodologies [6]. Similarly, investigations into droplet–wall interactions under varying conditions highlight the multifaceted nature of fluid–solid interactions [15–17].

Additionally, Mawarsih et al. [18] contributed to the understanding of droplet impact phenomena by conducting numerical simulations using Finite-difference and front-tracking methods. Their study, which focused on the impact of liquid droplets on horizontal solid surfaces, considered various parameters such as density ratio and gravitational effects. By validating their numerical results against experimental data, they underscored the pivotal role of gravity in governing maximum deformation diameter and spreading velocity, thereby enriching our understanding of droplet dynamics on solid surfaces.

In this pursuit of knowledge, experimental endeavors play a pivotal role. By meticulously recording droplet–wall collisions under controlled conditions, researchers generate invaluable datasets for benchmarking computational models. These experiments serve as touchstones for validating simulation outcomes and refining numerical methodologies.

In conclusion, the study of droplet collisions transcends disciplinary boundaries, encompassing a rich tapestry of physics, engineering, and computational science. As researchers continue to unravel the intricacies of these phenomena, they pave the way for transformative advancements in fields as diverse as energy, manufacturing, and environmental engineering.

2. Model Description

The model for physical and numerical experiments consisted of the formation of a liquid film by the impingement of droplets on a wall. The sketch of the experiment is illustrated in Figure 1. An injector generates a chain of droplets that collide with the opposite wall, forming the liquid film.
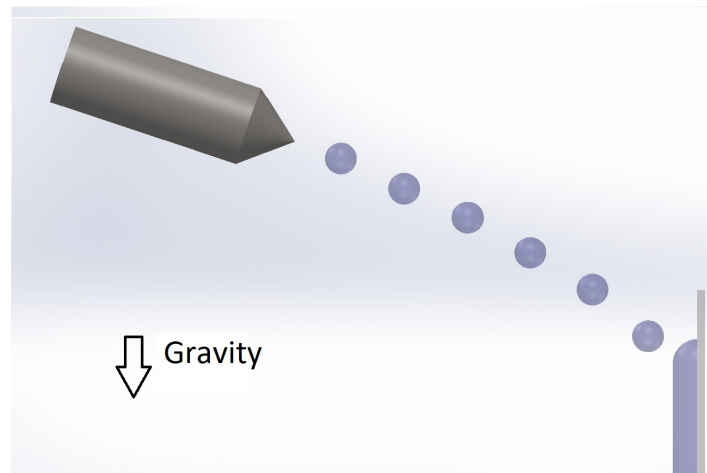

Figure 1. Representation of the liquid film formation.

The following sections will explain how this model is reproduced in physical and numerical experiments.

2.1. Experimental Test Rig

The experimental test rig is illustrated in Figure 2. The test rig consists of a droplet generator with an oscillating membrane (Encap BioSystems, model IE-0010H-P, Postack-erstrasse 10, 4710 Balsthal, Schweiz), which is responsible for generating a water droplet chain (in blue in Figure 2). This droplet chain impacts the opposite wall, where a liquid film forms (shown in red in Figure 2). For the physical experiment, two PHOTRON FAST-CAM SA4 cameras equipped with a Nikon lens PC-E Micro Nikkor (2 Chome-15-3 Konan, Minato City, Tokyo 108-0075, Japan) 85 mm 1:2 were used (represented in black in Figure 2). The first camera recorded the impinging droplets and the liquid film from a sideways perspective, while the second camera captured the shape of the film on the back of the transparent wall.
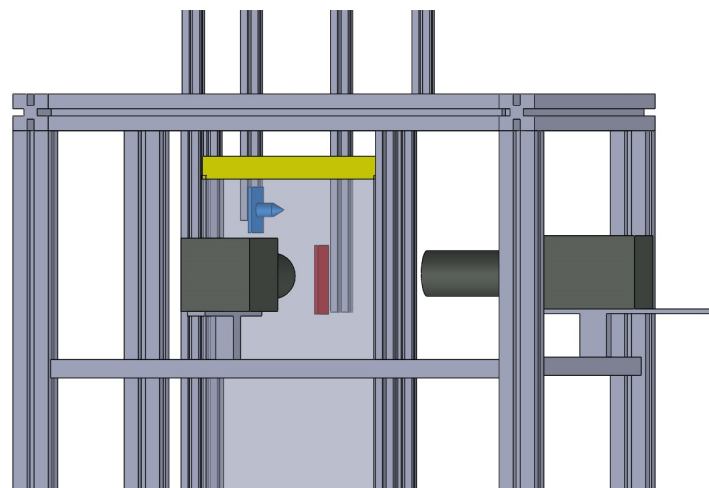

Figure 2. Illustration of test rig.

The amplifier (Thoman TA1050 MK-X, Thomann GmbH, Treppendorf, Hans-Thomann-Straße 1,D-96138 Burgebrach, Germany) was used to generate the amplitude of an oscillating signal for the actuator. This set of equipment was used to control the first break up of the liquid jet, generating a controlled droplet chain.

The injection system was pressurized by an Air Compressor Werther Model P 50/24 AL Black Panther (8614 Veterans Memorial Dr, Houston, TX 77088, USA). Compressed air was used to pressurize an Impexron GmbH vessel Krautzberger 200-0278 (Impexron GmbH Przemyslowa 2A 32-566 Krzeszowice, Poland), which contained the water.

A set of LED lights was assembled behind an opaque screen to diffuse the light. The system was powered by a programmable power supply Hameg Instruments HMP4030384 (HAMEG Instruments GmbH Wilhelm-von-Siemens-Str. 23 12277 Berlin, Germany).

A traverse system ISEL automation CNC controller C 116 was used to align the camera.

To measure the density of the liquid, volume and mass measurements were necessary. To measure the volume, a 50 mL volumetric flask (DIN 12797), Kirburger Weg 59, 50767 Köln, Germany was used. The empty volumetric flask was placed on a Sartorius electronic precision balance. It was then filled with liquid and weighed. The mass difference was the liquid mass. Using the measured volume and the calculated mass, it was possible to obtain the density of the liquid.

To measure the viscosity of the liquids, a Brookfield KF10 falling ball viscometer was used. The inner tube was filled with the liquid and a glass sphere was placed on the top side. By measuring the time it takes for the ball to reach the bottom, Equation (1) is used to calculate the dynamic viscosity.

$$\mu = t(\rho_1 \rho_2) KF, \tag{1}$$

where μ stands for dynamic viscosity, t denotes the traveling time of the ball, ρ_1 denotes the density of the ball, ρ_2 denotes the density of the liquid, K denotes the ball constant according to the test certificate, and F denotes the working angle constant (which is also found in the calibration certificate).

To measure the surface tension of the liquid, a ring tear-off method was used. The properties of the fluids are then presented as follows: Air is considered to have a density of $\rho_g = 1.427 \text{ kg/m}^3$ and a dynamic viscosity of $\mu_g = 1.7894 \times 10^{-5} \text{ kg/m} \cdot \text{s}$, at 300 K. Water has a density of $\rho_l = 994 \text{ kg/m}^3$, and a dynamic viscosity of $\mu_l = 7.35 \times 10^{-4} \text{ kg/m} \cdot \text{s}$, at 300 K. The surface tension between these phases is $\sigma = 0.0688 \text{ N/m}$. Ethanol has a density of $\rho_l = 783 \text{ kg/m}^3$, and a dynamic viscosity of $\mu_l = 9.05 \times 10^{-4} \text{ kg/m} \cdot \text{s}$, at 300 K. The surface tension between these phases is $\sigma = 0.0268 \text{ N/m}$.

The measured fluid properties are summarized in Table 1.

Table 1. Fluid properties at 300 K.

	Density (kg/m^3)	Dynamic Viscosity (kg/m $\cdot$ s)	Surface Tension Coefficient (N/m)
Air	1.427	1.7894×10^{-5}	-
Water	994	7.35×10^{-4}	0.0688
Ethanol	783	9.05×10^{-4}	0.0268

For image processing, an open-source ImageJ-based processing package called Fiji was used. In order to analyze each droplet, a Fiji package named "Analyse particles" was used.

This package returned the values of circularity and the centroid position of each droplet. Knowing the time between two captured images and the centroid of a droplet in each image, it was possible to calculate the velocity. To calculate the impact angle, the velocity vector was used. The angle between the velocity line and the wall was considered as the impact angle of the droplet. A script was generated to automatically analyze the droplet collision using Fiji; it is available for other users for modification and use freely [19]. It is available at de Lima [19].

2.2. Numerical Model

For the numerical simulations, three cases were selected among the physical experiments to be reproduced using the VOF method. A parallelepiped surface mesh (6 mm width, 10 mm length, and 16 mm height) was created using Convergent Science Inc.'s CONVERGE^{TM} CFD software version 3. Such a surface corresponds to the image area of the experiment, as seen in Figure 1. Three spheres were created inside the domain, representing the region where the droplets were initialized, with their velocity magnitude and direction corresponding to physical experiments. Incoming droplets, with the same velocity and diameter, entered the domain via the top boundary. The simulations ran until water flew out of the computational domain through the bottom boundary. Droplets then performed a diagonal trajectory, colliding against a vertical wall. Two techniques were used to locally refine the mesh. The first technique was used to refine the regions where droplets were initialized as well as the wall regions. These embedded spherical regions refine the mesh by a factor of 2^n. For the simulations, n was set to 4. These embedded regions for the droplets were used only at the beginning of the simulations. To keep track of the liquid–gas interface, a second technique called adaptive mesh refinement (AMR) was used. This technique tracks cells with void fraction (α) values between 0 and 1, indicating that the cell contains an interface. In these cells, the mesh was locally refined by a factor of 2^n; for the simulations, n was also set to 4 for the AMR technique. The base size was 0.3 mm. In both techniques, in the regions chosen to be refined by the criterion of 2^n, the base mesh size was 0.01875 mm. The time step was also variable according to predefined values. The minimum time step value was set to 10^{-7} s and it was adjusted for each time step automatically. Gravity was set to $9.81, \text{m/s}^2$ in the y direction.

The volume of fluid (VOF) method is used to track the interface between fluids. In this method, the void fraction (α) of each cell is calculated throughout the computational domain. This variable calculates the amount of each fluid contained in a cell. The volume fraction value can be found in three different situations: 0—representing only the first fluid considered in the cell, 1—representing only the second fluid, or the value can be between 0 and 1—representing both fluids. The third situation indicates the existence of the interface between the fluids.

The mathematical model for this approach can be described by Equations (2)–(6). The mass balance equation in the VOF method for incompressible two-phase systems is presented in Equation (2). The momentum balance is presented in Equation (3). The transport equation for the volume fraction (α) is presented in Equation (4). Density and viscosity are calculated in Equations (5) and (6), respectively, as a function weighted by the volume fraction (α) contained in the cell, as adapted from [20].

$$\nabla \cdot u = 0, \tag{2}$$

$$\rho \left[\frac{\partial u}{\partial t} + u \cdot \nabla u \right] = -\nabla p + \nabla \cdot \left[\mu \nabla u + \mu (\nabla u)^T \right] + \rho g + F_{sfi}, \tag{3}$$

$$\frac{\partial \alpha}{\partial t} + u \cdot \nabla \alpha = 0, \tag{4}$$

$$\rho = (1 - \alpha)\rho_l + \alpha \rho_g, \tag{5}$$

$$\mu = (1 - \alpha)\mu_l + \alpha \mu_g, \tag{6}$$

in which t denotes time, ρ_g denotes gas density, μ_l denotes the dynamic viscosity of the liquid, and μ_g denotes the dynamic viscosity of the gas. F_{sfi} denotes the force related to

the surface tension. This surface tension force is modeled using a continuum surface force (CSF) model in the present work, as indicated in Equation (7).

$$F_{sfi} = \sigma \kappa(x) \frac{\partial \tilde{\alpha}(x)}{\partial x_i},\tag{7}$$

where σ denotes the surface tension coefficient, κ denotes the local curvature of the interface, and n denotes the unit normal to the interface. Computing κ requires the local curvature, which is calculated according to Equation (8).

$$\kappa = -\frac{\partial n_i}{\partial x_i},\tag{8}$$

n_i is the surface curvature, calculated at the interface according to Equation (9).

$$n_i = \frac{\frac{\partial \alpha}{\partial x_i}}{\left|\frac{\partial \alpha}{\partial x_i}\right|},\tag{9}$$

For modeling the fluid interaction of the wall, the contact angle adjusts the normal vectors of the cells close to the wall as in the model developed by Brackbill et al. [21]. The curvature of the surface near the wall is then adjusted to the boundary condition. The surface normal at the cell next to the wall is calculated as in Equation (10).

$$n_i = n_{wi}cos(\theta_w) + t_{wi}sin(\theta_w),\tag{10}$$

in which θ_w is the contact angle on the wall, and n_{wi} and t_{wi} are the unit vectors normal and tangential to the wall, respectively. The local curvature of the surface is determined by the combination of this contact angle and the calculated normal vector. This curvature is used to adjust the body force in the surface tension equation.

A modified void fraction is defined in Equation (11). This modified void fraction is used to compute the force.

$$\tilde{\alpha}(x) = \frac{1}{h^3} \int_V \alpha(x')\phi(x' - x)d^3x',\tag{11}$$

in which $\phi = 0$ for $|x| \geq h/2$, and h is a thickness across the interface between fluids.

There are a considerable number of numerical schemes available for interface tracking. Explicit methods are generally less stable due to their reliance on small time steps. Accuracy depends on the quality of the interface reconstruction and the chosen numerical scheme. While explicit methods can capture complex interfaces, they may suffer from numerical diffusion. Implicit methods are more stable, enabling larger time steps. Accuracy is maintained even with larger time steps due to the matrix inversion approach. However, implicit methods may slightly smooth the interface.

Among the many options, the coupled level-set VOF (CLSVOF) stands out as it combines the advantages of both VOF and level-set methods. It uses the level-set function to represent the interface and couples it with the VOF method. The level-set function provides accurate interface geometry, while VOF handles mass conservation. Nevertheless, this method was not available in the computational code used in the present work. For further details on the surface reconstruction methods used with the VOF method, the reader is encouraged to read references [8,20], to name just a few.

In this paper, two different schemes were used, namely, high-resolution interface capturing (HRIC) and piecewise-linear interface calculation (PLIC). The HRIC scheme was introduced as an improvement over existing methods, aiming to strike a balance between accuracy and stability. It essentially blends bounded downwind and upwind differencing schemes to enhance interface capturing. By controlling the upwind and downwind differencing schemes, HRIC achieves a more accurate representation of the interface. Unlike some methods that explicitly depend on the Courant–Friedrichs–Lewy (CFL) condition, HRIC avoids this limitation. On the other hand, the PLIC method is

purely geometrical and aims to accurately capture and track fluid interfaces within a computational domain. It is particularly useful for scenarios involving multiple fluid phases (e.g., liquid–gas, liquid–liquid), where the interface between them needs precise representation. Unlike some other methods, PLIC focuses on maintaining a sharp interface while minimizing numerical diffusion. It constructs the interface by approximating it as a piecewise linear function across grid cells.

3. Results and Discussions

In this section, the results of the physical experiments and the results of the numerical simulations are presented. The results are then compared and the physics of the phenomenon is analyzed.

3.1. Physical Experimentation Results

In this subsection, the main results from the physical experimentation are presented and discussed. First, the results are qualitatively discussed. Subsequently, the quantitative results are illustrated and discussed.

For the liquid film formation tests, three different nozzles were used. The difference lies in the diameter of the hole, with sizes of 0.4 mm, 0.3 mm, and 0.2 mm. These tests were conducted in a quiescent environment.

Considering cases of complete absorption of the droplet in the liquid film, some important observations are illustrated in the images that represent the pool formation. Taking, for instance, the example of droplets generated by the 0.3 mm nozzle, outcomes are droplets with an average diameter of 0.85 mm and velocity magnitude of 3.6 m/s (Reynolds = 3428 and Weber = 151) in an impact angle of 70°. The impact is represented in the sequence of images in Figure 3, which demonstrates the pool formation. Figure 3a represents the incoming droplet just before the impact. After the impact, the droplet spreads radially as presented in Figure 3b, spreading the liquid film. Gravity acts downward while surface tension acts to regroup the liquid, The results of these forces are presented in Figure 3c, in which the droplet spreading reaches the sides of the a pool, where the liquid height is maximum. Then, this added mass is carried downward, as presented in Figure 3d, forming a narrower, and thicker film.


(**a**) (**b**) (**c**) (**d**)
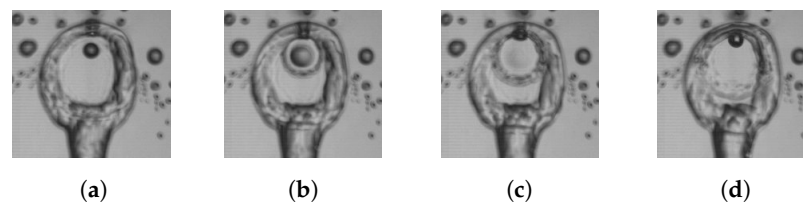
Figure 3. Droplet collision on wall.

Using the traverse system for the camera, different impact angles could be analyzed. The camera was adjusted to capture at a frame rate of 10,000 fps. Figure 4 shows different pool shapes depending on the impact angle. Figure 4a shows the impact generated by droplets with an average diameter of 0.38 mm and velocity magnitude of 2.05 m/s (Reynolds = 873 and Weber = 22) at an impact angle of 56°, and Figure 4b shows the collision of droplets with an average diameter of 0.33 mm and a velocity magnitude of 2.25 m/s (with Reynolds number = 832 and Weber number = 23) at an impact angle of 46°. Notably, an increase in the impact angle results in a pool with a smaller aspect ratio. This behavior was anticipated, as the impact angle is directly related to the velocity components. For instance, consider two equal droplets with the same velocity magnitude but different impact angles. The droplet with a higher impact angle experiences a greater velocity in the gravity direction and a smaller velocity perpendicular to the wall. Consequently, less energy is expended in the spreading of the droplet.
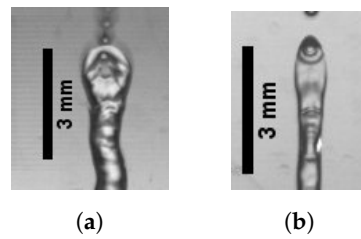
Figure 4. Pool shape dependence on the impact angle.

By changing the flow rate at the valves and adjusting the cutting frequency, it was possible to change the velocity of the impinging droplets. Taking the example of the impact generated by droplets with an average diameter of 0.62 mm and velocity of 2.1 m/s (Reynolds = 1459 and Weber = 37) at an impact angle of 60°, the pool is illustrated in Figure 5a. For an average diameter of 0.81 mm and velocity of 2.71 m/s (Reynolds = 2459 and Weber = 82), at an impact angle of 66°, the pool is presented in Figure 5b. For an average diameter of 0.85 mm and velocity of 3.36 m/s (Reynolds = 3199 and Weber = 132), at an impact angle of 69°, the pool is presented in Figure 5c. It can be observed from the images that by increasing the velocity, the aspect ratio of the pool also increases. This behavior was also expected since the velocity perpendicular to the wall increased, so more energy was used to spread the droplet.
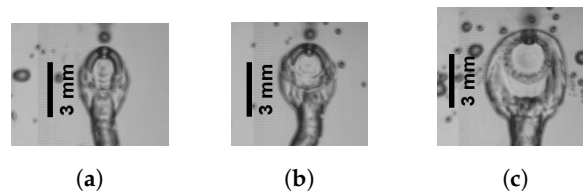
Figure 5. Pool shape dependence on droplet velocity.

The outcomes of the droplet impingement on the wall can be categorized into three main types, as depicted in Figure 6a–c. The droplet diameter is 0.85 mm, corresponding to Reynolds and Weber numbers of 3428 and 151, respectively. Figure 6a presents the striping of the droplet. In this condition, the incoming droplets hit the wall and begin film formation, but part of the droplet mass is stripped out. Figure 6b presents the bouncing, in which the impinging droplets touch the wall, but the liquid film is not formed and the droplets are bounced in the opposite direction of the impingement. Figure 6c depicts complete absorption, where impinging droplets are entirely absorbed by the forming liquid film. The behaviors observed in Figure 6a,b, are notably influenced by the momentum parameter, which was approximately 13.74 in this study. Note that lower values of the momentum parameter correlate with a higher likelihood of partial deposition.

As the velocity of the droplets increased, the splashing phenomenon was observed as in Figure 7. As the secondary droplets exited the camera's focus, measurements were not feasible using this technique. To measure the secondary droplets, a method akin to the one described in [22] should be employed. In this context, the laser Doppler anemometry (LDA) technique is recommended.

(**a**)
Striping

(**b**)
Bouncing

(**c**)
Absorption
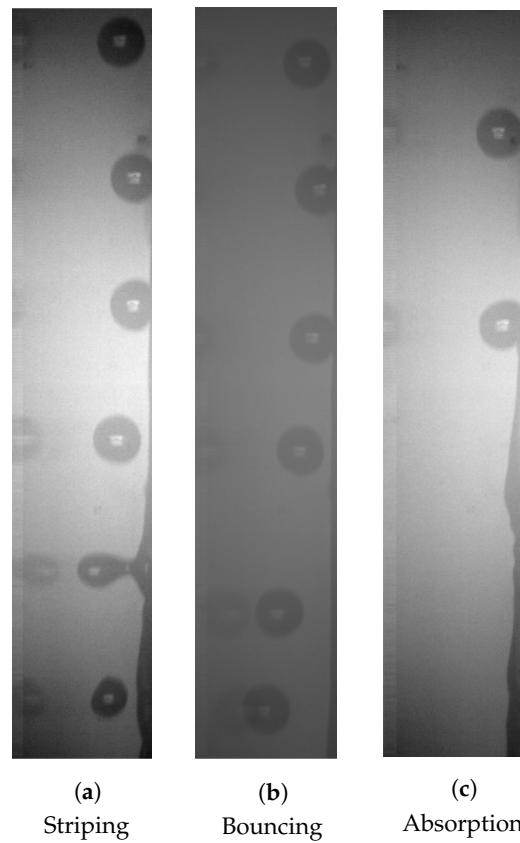
**Figure 6.** Possible outcomes from droplet collision.
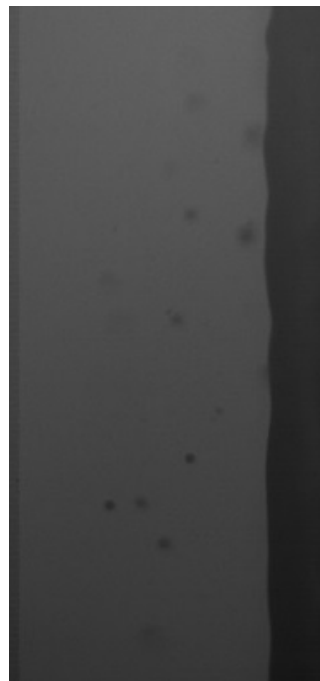
Figure 7. Image of splashing.

Quantitative results were obtained through the following procedure: The droplets were initially generated at a specific angle, and then this angle was systematically varied to achieve different impact angles. By adjusting the impact angle, we could determine the maximum angle at which partial deposition occurs. Next, the flow ratio was varied, and the impact angle was once again assessed to identify the maximum angle before

partial deposition. This same procedure was applied for different nozzle sizes. The primary outcomes are summarized in terms of a set of dimensionless numbers in Figure 8. This figure is a graph of the dimensionless number represented in Equation (12) and in Equation (13) for the tested cases. Equation (12) represents a dimensionless pool size, which is the actual pool size, which is the maximum width of the liquid film, over the incoming droplet diameter. Equation (13) represents the momentum parameter (S_{cd}), also called the spreading coefficient, for the primary droplets. This parameter is also used to predict the outcome of droplet impingement. As illustrated in Equation (13), the momentum parameter is a combination of the Reynolds number and the Laplace number, the last being a combination of the former and the Weber numbers. As explained by Samenfink et al. [22], this momentum parameter is used to analyze the outcomes of droplet impingement over walls. In his work, this parameter is used to predict the droplet outcome from the collision. If this parameter is low, the droplet coalesces and is completely absorbed by the film liquid. For high momentum parameter, the droplet is broken up and generates secondary droplets. As this dimensionless number is a combination of the Reynolds number and Laplace number, it can be interpreted as a combination of the fluid momentum force to viscous shear force ratio and the surface tension to momentum transport ratio.

$$w_0 = \frac{w}{d_0}, \tag{12}$$

$$S_{cd} = \frac{1}{24} \frac{\rho_l^{0.581}}{\mu_l^{0.162} \sigma^{0.4189}} d_0^{0.581} v_d \sin^{0.63}(\alpha_{impact}) = \frac{1}{24} Re La^{-0.4189}, \tag{13}$$
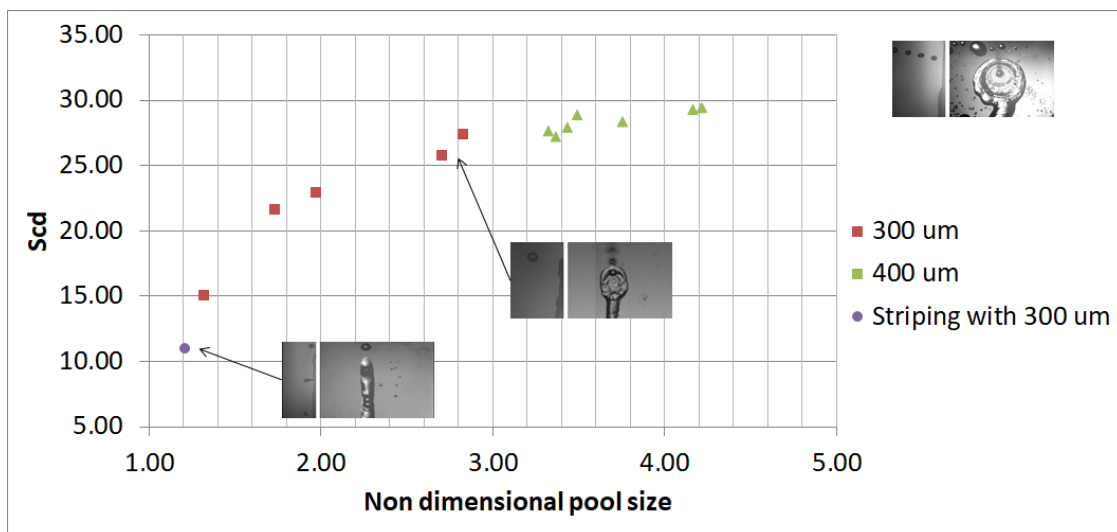

Figure 8. Scd versus non-dimensional pool size.

The Laplace number, in turn, represents a surface tension to momentum transport ratio (especially dissipation) inside a fluid and is calculated using Equation (14).

$$La = \frac{\sigma \rho d_0}{\mu_l^2} \tag{14}$$

Analyzing the data in Figure 8, it is possible to conclude that the results exhibit a logarithmic trend. As the non-dimensional pool size approaches values close to one (indicating that the pool size is approximately the same as the droplet diameter), striping is more likely to occur. Notably, for high values of the momentum parameter (25 and above), even a small variation in the momentum parameter leads to a significant change in the non-dimensional pool size.

For ethanol, a distinct behavior was observed. Upon collision, the droplets spread into a significantly wider pool, as evident in Figure 9a,b. Unfortunately, the pool size was not

directly measured, preventing the establishment of a correlation between the spreading coefficient (Scd) and the pool size for this specific case.


(**a**)　　　　　　　　　(**b**)
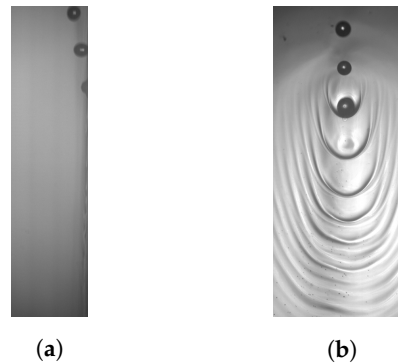
Figure 9. Collision visualization for ethanol. (**a**) Ethanol droplets (side view), (**b**) Ethanol droplets (front view).

A set of outcomes for droplet impingement is summarized in Table 2. When observing the behavior of water droplets, the highest value found for a partial deposition condition was 13.74, while the smallest value for complete absorption was 15.06. Similar behavior was observed for ethanol. Critical values for partial deposition were around 17, but for ethanol, this number had an interference range between 15 and 20, within which both partial and total depositions were observed.

Table 2. Outcome of droplets.

Water		Ethanol	
Scd	Outcome	Scd	Outcome
29.44	Absorption	22.35	Absorption
25.76	Absorption	15.23	Absorption
21.58	Absorption	17.73	Partial deposition
15.06	Absorption	16.89	Partial deposition
13.74	Partial deposition	16.13	Partial deposition
11.26	Partial deposition	15.04	Partial deposition

To complete the physical experimentation, a small droplet was placed on a horizontal plate for the droplet contact angle measurement. Using the algorithm created by [23] for Fiji, a contact angle of 78.5° was calculated, as presented in Figure 10a,b. This contact angle was used for the numerical modeling.

(**a**)　　　　　　　　　(**b**)
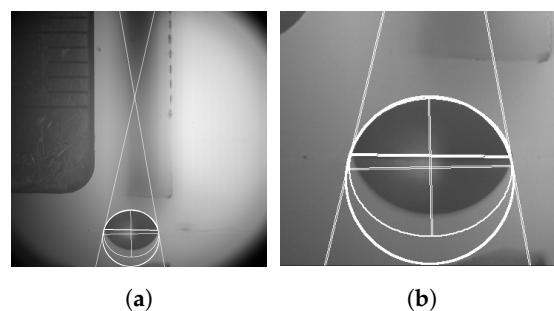
Figure 10. Contact angle measurement. (**a**) Representative lines for the contact angle calculation on the full image, (**b**) representative lines for the contact angle calculation near the droplet and its reflex.

3.2. Numerical Findings

In this section, the numerical results are presented. First, the case setup is explained and then the results are presented.

3.2.1. Numerical Setup

The mesh generated for the simulations is illustrated in Figure 11. As observed in this figure, the mesh was initially refined at the inlet boundary, where the droplets were issued, and at the wall where the droplets impinge. Inside the domain, the initial droplets are depicted, along with an incoming droplet issuing from the boundary condition. For the simulated cases, the droplets have a diameter of 0.645 mm, consistent with the experiment reproduced by the current simulations. To achieve different momentum parameters, the velocity magnitude was kept constant, but the direction was altered. In the simulations, the void fraction value was defined as one for the gas phase and zero for the liquid phase. The air phase was considered quiescent during initialization. The liquid and gas properties used for the simulations are presented in Table 1. A contact angle of 78.5° was employed, as calculated using the experimental setup. The HRIC and PLIC schemes were utilized, and their results are discussed in this subsection.
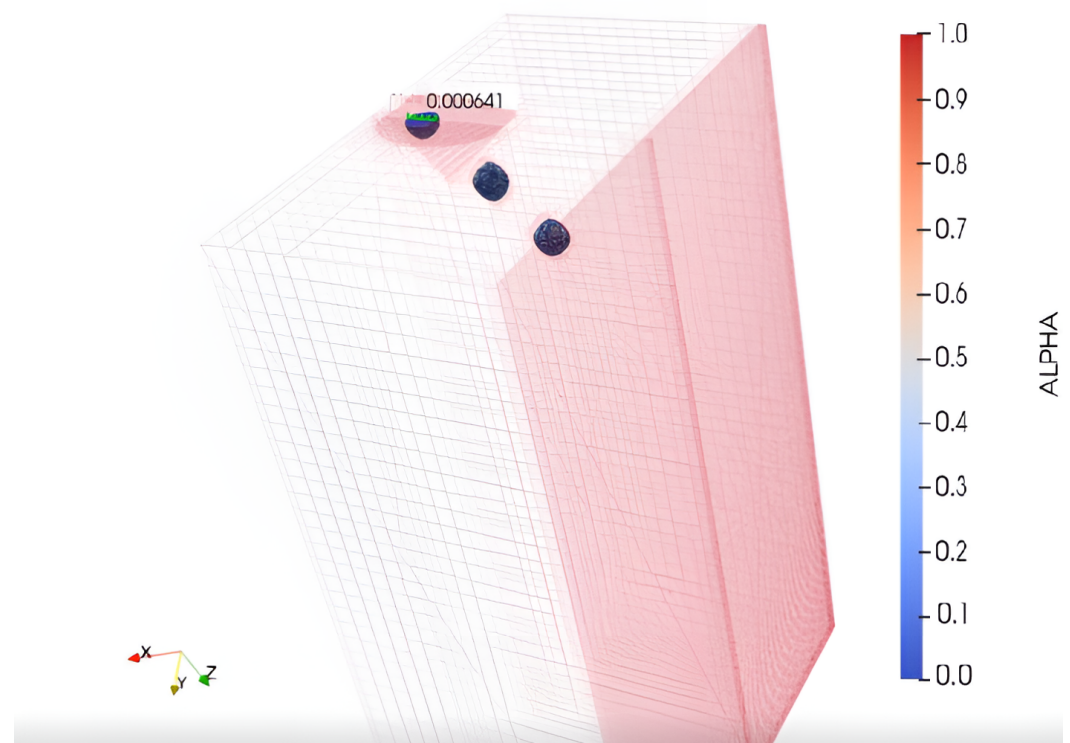
Figure 11. Initial setup.

The initial embedded regions for droplets are depicted in Figure 12. Initially, both droplet and wall regions were initialized with a smaller resolution for cell size. To enhance simulation efficiency, the wall refinement was retained, but the initial droplet refinement was removed after a few time steps. As the droplets moved through the computational domain, further refinement for the droplet regions was performed using AMR, as shown in Figure 13. Notably, inside the droplet, the mesh is not as finely refined as at the interface between fluids. Additionally, the refined region extends beyond the droplet interface boundaries. This behavior occurs because AMR has also been applied to the velocity field, as presented in Figure 14. In summary, the AMR technique was employed to refine regions where there was variation in the volume fraction or velocity field.
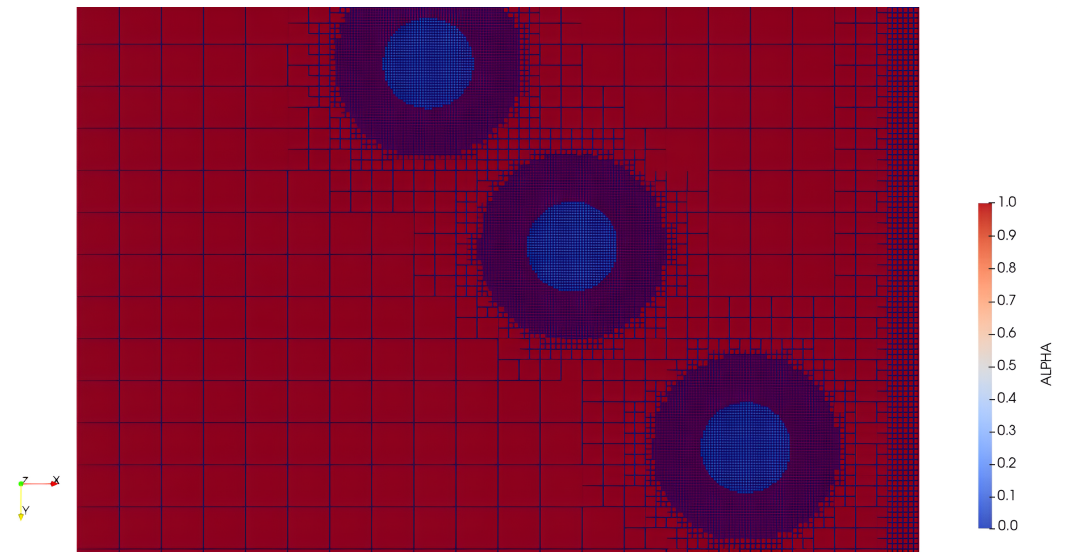
Figure 12. Embedded regions.
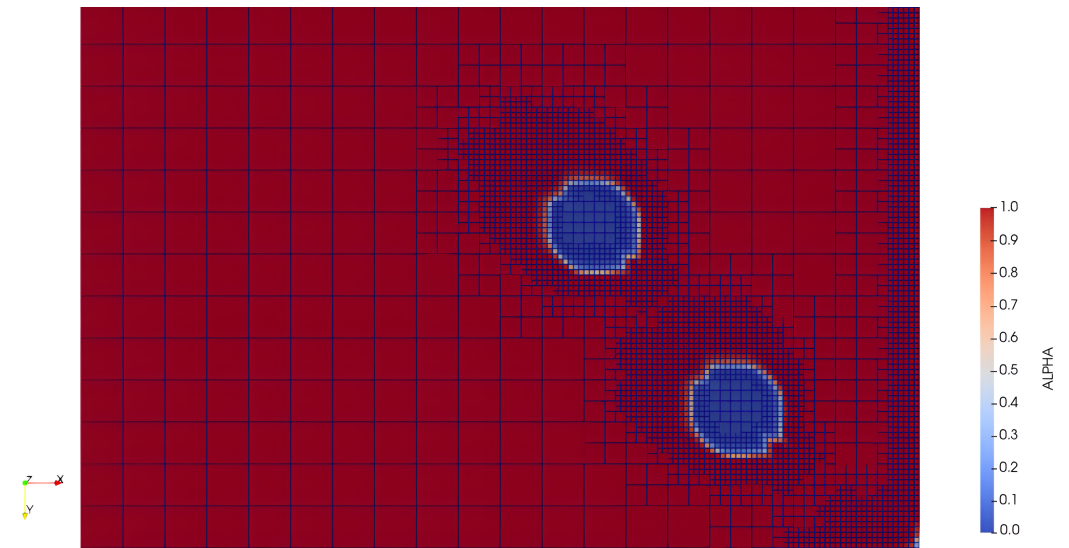
Figure 13. Adaptive mesh refinement of the droplet.
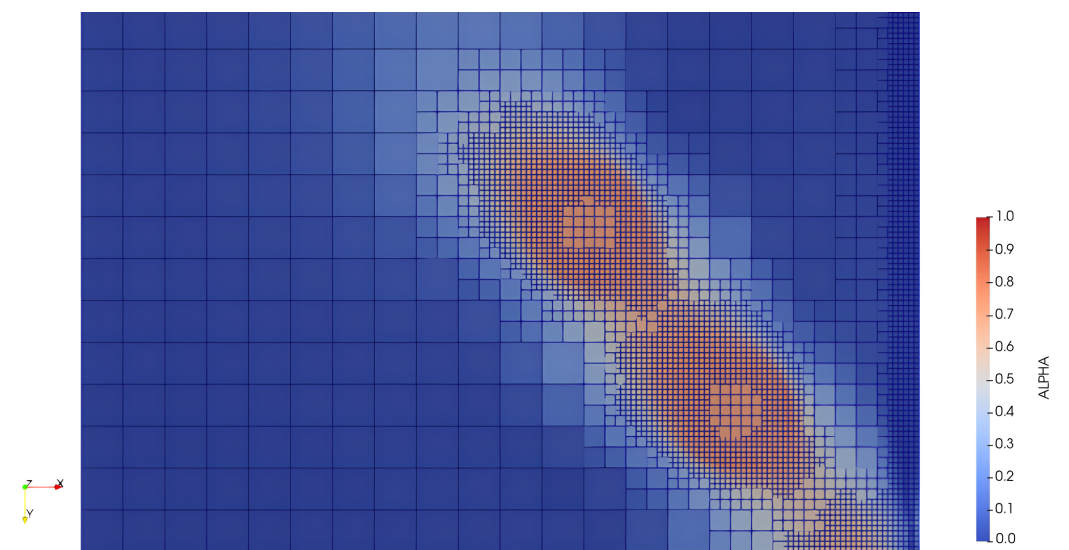

Figure 14. Adaptive mesh refinement for velocity.

At this stage, it is important to emphasize that the PLIC simulations were not stable enough to deal with the initial discontinuities. The droplets inside the domain were set with an initial velocity and the air around them was quiescent. Even for small time steps and for very fine meshes, the discontinuities of the simulation setup caused the PLIC simulations to diverge. The simulations for the PLIC scheme were then run only with incoming droplets from the inlet boundary region. This was not the case for the HRIC simulations, which were able to handle the discontinuities.

For the simulations, the adaptive time step was used. The variations were dependent on the CFL number and exhibited significant differences for HRIC and PLIC simulations. For the HRIC scheme, the simulations were run with a time step of approximately 5×10^{-6} s, while the simulations using the PLIC scheme were run with a predefined minimum time step of 1×10^{-7} s, which means that it would require even smaller time steps. These findings are in contrast with the results observed for flows aligned with the mesh presented by de Lima et al. [8].

3.2.2. Numerical Results

To visualize the computational effort required for the simulations, a graph was generated for an HRIC simulation. This graph includes the number of cells and memory usage in MB, as shown in Figure 15. For the sake of brevity, the results are presented only for HRIC, as the graph for PLIC behaves similarly. The main difference is that, for the same setup, HRIC required more cells than PLIC (approximately 1.5 million cells for HRIC compared to 1.1 million cells for PLIC). This resulted in a greater memory requirement for HRIC simulations (around 9.2 GB for HRIC compared to 7.5 GB for PLIC). Additionally, the graph shows that simulation requirements and the number of cells increase with simulation time due to the adaptive mesh refinement, which generates more cells during film formation and the issuing of new droplets. This behavior continued until there was a flow out of the computational domain, at which point the simulation reached a maximum number of cells and then stabilized. Note that there was an increment of more than 50% in the number of cells.
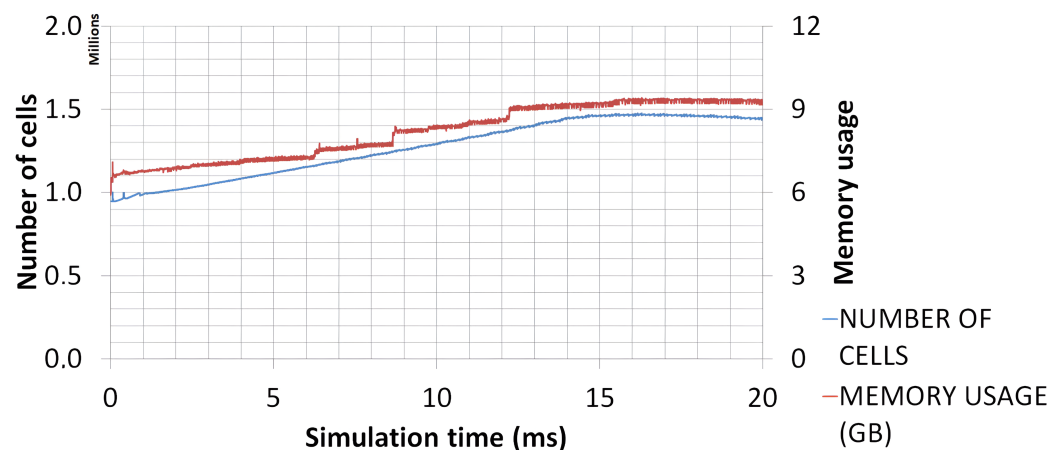

Figure 15. Number of cells and memory usage for the VOF simulations using AMR. As the droplets enter the computational domain, the number of cells required to simulate the interface increases and so does the memory usage.

For numerical validation purposes, three cases were chosen to build a graph similar to Figure 8. The case with the smallest Scd is called Case 1, the second smallest Scd is called Case 2, and the case with the greatest Scd is called Case 3. For this set of physical and numerical experiments, the droplet size was kept constant and its diameter was 0.645 mm. The same procedure was then carried out for the simulation cases, with the impact angle changed. The results are summarized in Figure 16, which contains the results of the numerical simulations. For the first set of simulations presented in this figure, only half

of the domain was used to save simulation time, except for the simulation marked with a black square, which was run to test the symmetry boundary condition approximation. The results are qualitatively discussed throughout this section.

These cases were chosen to cover the range of the experiment, from partial deposition (Case 1) to medium cases where the Scd parameter directly influences the pool size (Case 2), and to cases where a small change in the Scd parameter value results in a large variation in the pool size (Case 3).

From Figure 16, it is observed that in Case 1, both schemes presented very similar results regarding the dimensionless pool size. The difference between the experimental and numerical results is partially explained by the fact that neither scheme could predict the partial deposition expected in this case. For Case 2, both schemes presented very good agreement with the experimental results. In Case 3, it is noteworthy that both schemes under-predicted the results of the physical experiments, which contradicts the findings in the other two cases. To further investigate this discrepancy, test cases were conducted for each of the two methods with the wall model disabled. As anticipated, the results deviated even further from the physical experiment.
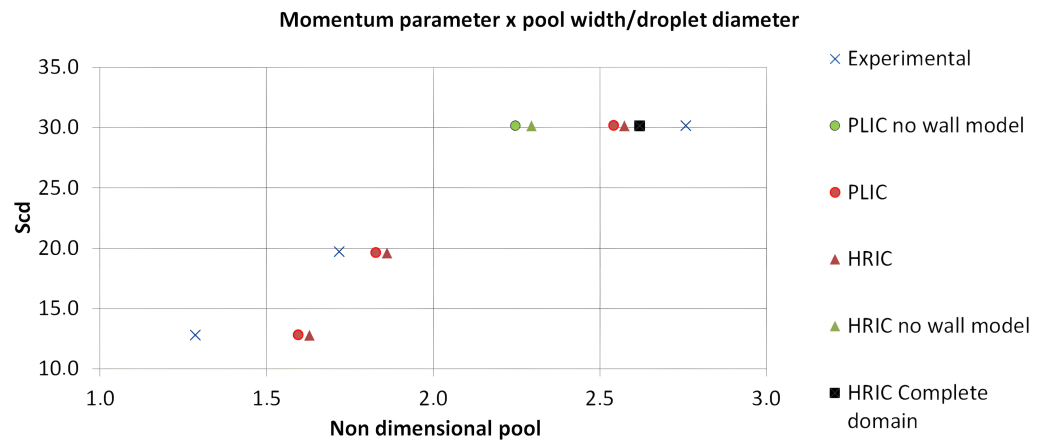
Figure 16. Comparison of the pool size between the numerical and physical experimentations.

To analyze the shape of the droplets generated for each scheme, Figure 17 was generated for the PLIC and HRIC schemes, shown on the left and right sides, respectively. To track the interface between the fluids, a sampling line was drawn vertically in the middle of the droplet, as illustrated in Figure 17a, and the values of α were plotted along this line in Figure 17c for the PLIC scheme. The same procedure was followed for the HRIC scheme in Figure 17b,d.
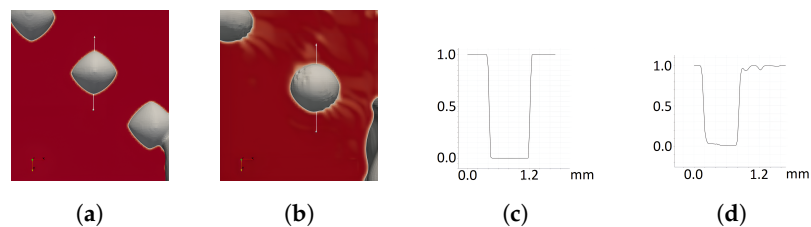

Figure 17. Droplets for PLIC and HRIC schemes.

The HRIC scheme exhibits numerical diffusion, evident from the interface smearing in Figure 17b. The AMR algorithm also refines the mesh in this smearing region for the HRIC scheme, which contributes to increasing the number of cells. This effect is also clear in the graph illustrated in Figure 17d, where instabilities near the interface are observed. The underlying cause lies in the approach used to reconstruct the interface between the fluids within the HRIC scheme, as detailed in the Numerical Model section.

No virtual numerical diffusion is observed in the PLIC scheme as shown in Figure 17c. This behavior is due to the purely geometric interface reconstruction of the scheme. Also, the droplet shape for this scheme was disturbed by the non-alignment of the droplet velocity and the Cartesian mesh. The droplet approached a diamond shape instead of a sphere. This poor prediction of the droplet shape leads to the formation of the pool in a similar way. The pool formation after droplet impingement on the wall is illustrated for Case 3 using the PLIC scheme in Figure 18 and HRIC in Figure 19. These images illustrate the results of the simulations considering half of the domain with a symmetry boundary condition. Notably, the pool shape in the PLIC scheme closely resembles a diamond shape similar to the form of the impinging droplet. On the other hand, the prediction of the HRIC scheme was more rounded and, therefore, closer to the shape captured by the images of the physical experiment. To enhance visualization, the images are reflected along the symmetry boundary condition, marked by the white line in the middle of each image.
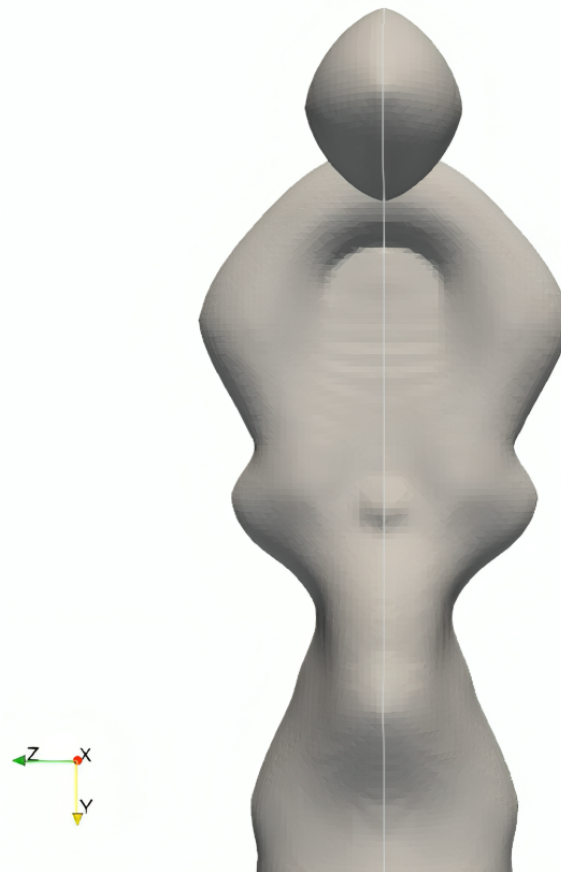

Figure 18. Pool shape for the PLIC scheme simulation considering half of the domain.
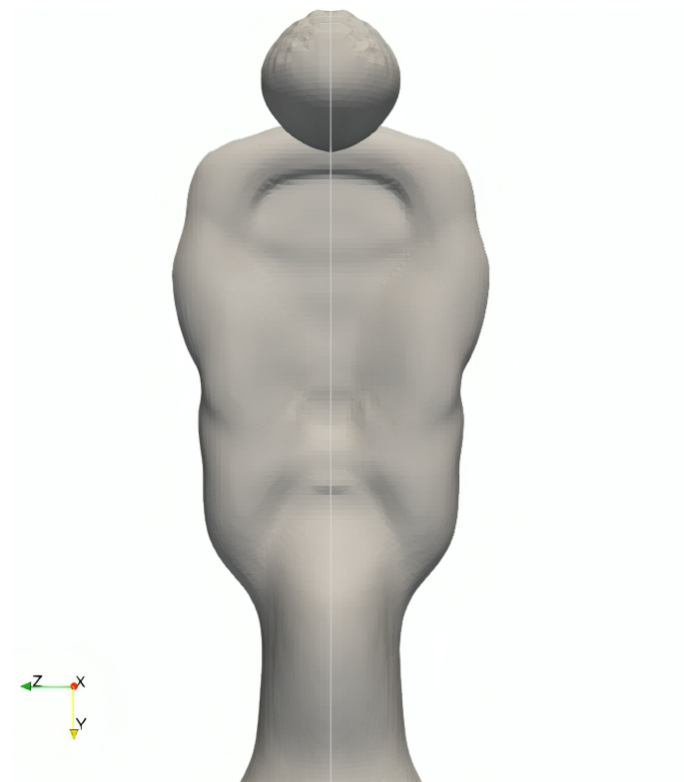
Figure 19. Pool shape for HRIC scheme simulation considering half of the domain.

Simulations were carried out with the complete domain; the results are illustrated in Figure 20 for PLIC and Figure 21 for HRIC. The simulations run with the PLIC scheme on the complete domain also presented the diamond pool shape. The pool shape formed by the HRIC scheme was different, appearing less spread along the y-axis and slightly wider. This difference is observed in Figure 16, where the simulation considering the complete domain is marked with a black square.
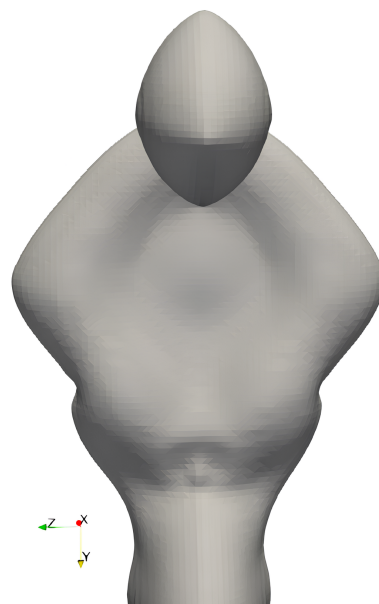
Figure 20. Pool shape for PLIC scheme simulation considering the complete domain.
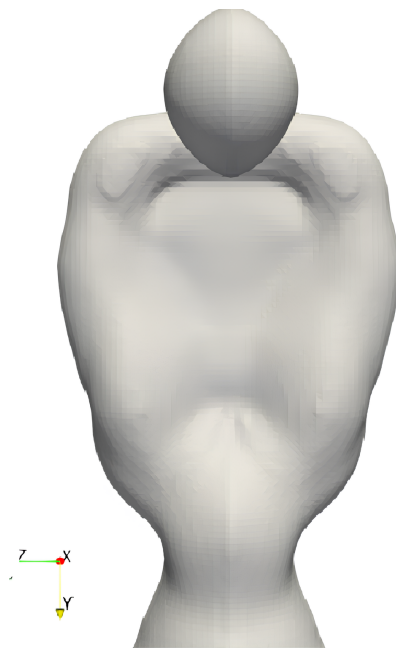
Figure 21. Pool shape for HRIC scheme simulation considering the complete domain.

To address the mesh problems arising from misalignment, an inlaid mesh is currently under development to optimize the PLIC scheme. This mesh is non-Cartesian and is generated within the computational domain. Typically, this mesh type is used to align with a known flow direction. Although it is still in development, it does have a few limitations. A more comprehensive analysis of the entire phenomenon related to pool formation will be conducted for the PLIC scheme after the new implementations.

The HRIC scheme presented a droplet shape closer to the images from physical experiments. Considering this, the HRIC scheme was chosen to proceed with the liquid film formation analysis.

The results for the simulation considering half of the domain and the complete domain are analyzed. The results for each of the approaches are presented in Figure 22, with results for the half domain mirrored along the white centerline for better visualization. As can be observed in the images, the shape of the pool changed when the symmetry condition was used, becoming more spread along the symmetry boundary. A comparison with the liquid film shape obtained from the physical experiment was carried out and is presented in Figure 23. In this image, it is possible to see that the shape resulting from the simulation considering the complete domain is closer to that of the physical experiment.
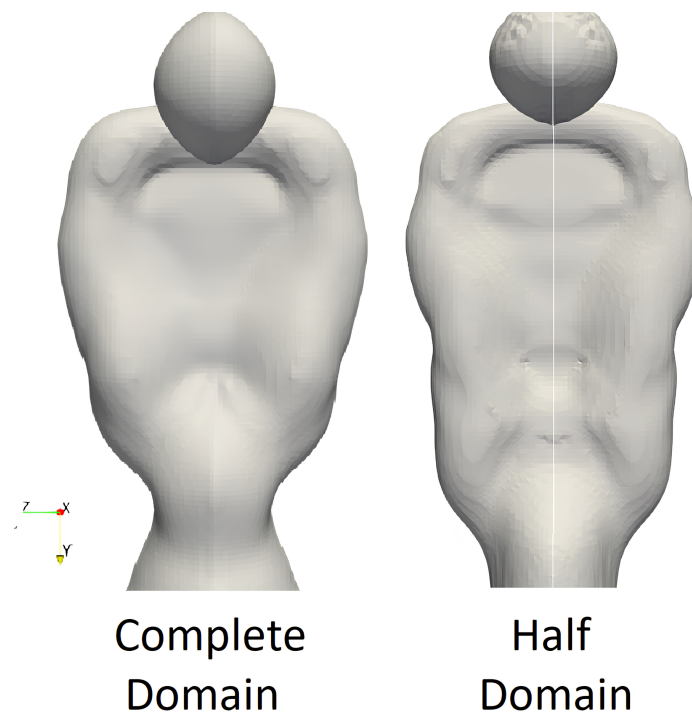
Figure 22. Comparison of the simulations using the full domain and half domain for the HRIC scheme.
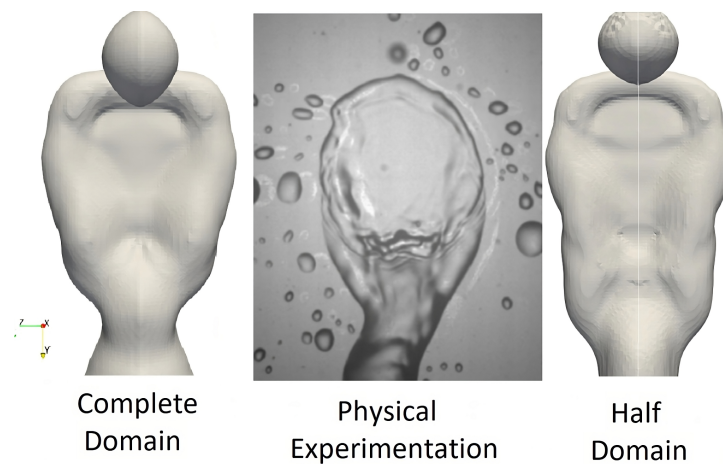

Figure 23. Comparison of the simulations using the HRIC scheme and physical experimentation.

To better understand the difference between the two approaches, Figure 24 was generated to represent the wet area in blue with the velocity vectors sized by velocity. The simulation with half the domain is illustrated on the left side of the image, and the results for the complete domain are on the right side. It can be noted that the widths of the pools are similar, but the results for the half domain show higher velocities in the y direction. This higher velocity causes the liquid to spread faster on the wall, forming a longer shape than expected and slightly decreasing the pool width.
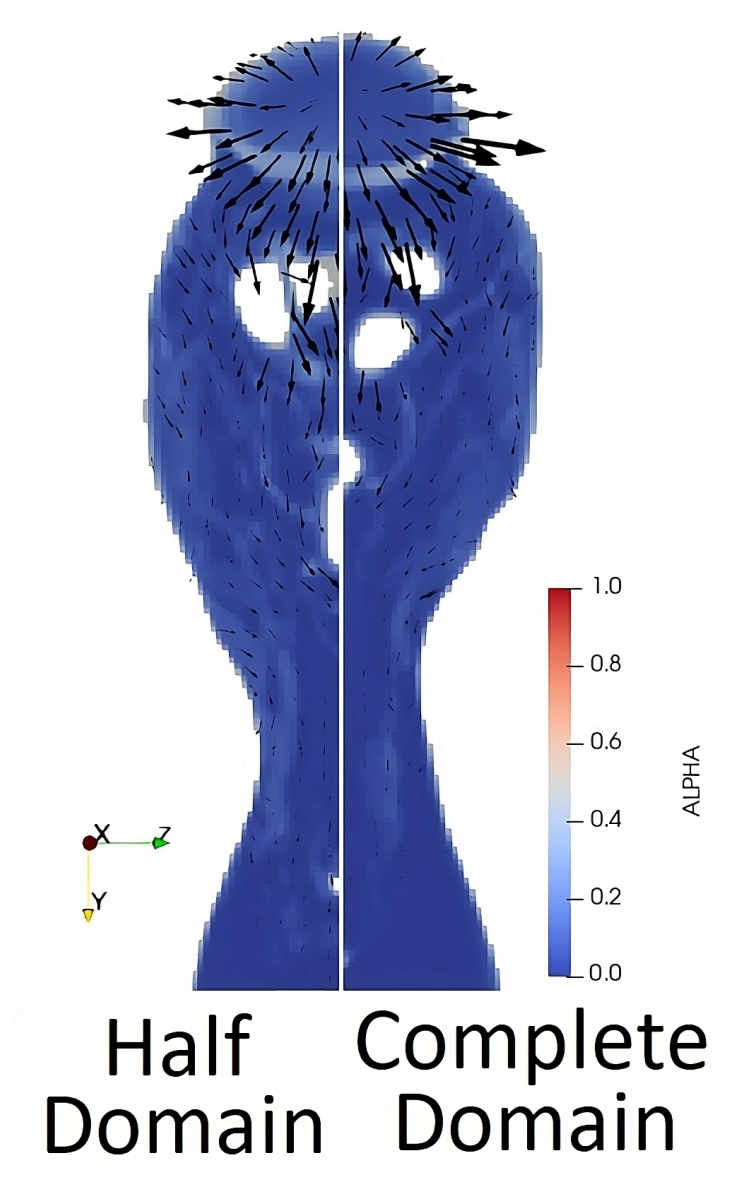
Figure 24. Comparison of the simulation using the complete domain and half of the domain for the HRIC scheme with velocity vectors.

4. Final Remarks

The main findings can be summarized as follows:

- A correlation was found for the Scd and the non-dimensional pool size for different droplet sizes and impact angles.
- Regions where partial depositions were most likely to occur were found by means of physical experiments.
- The PLIC scheme can maintain a sharper interface than the HRIC scheme.
- The simulations run using the PLIC scheme were not able to predict the round shape of the droplets in a Cartesian mesh with an unaligned flow. To solve this issue, the inlaid mesh was under development.
- For the cases investigated in the present work, the PLIC scheme required a smaller time step. These results are opposed to previous results presented for flows aligned with the Cartesian mesh.
- The HRIC scheme was more stable than the PLIC considering the initial discontinuities.
- The symmetry boundary condition imposed in the middle of the computational domain is not suitable for the high momentum parameter.

Data Availability Statement: A script to analyze droplet images is available at https://github.com/brunosdlima/CFD/tree/c918293ab9dec1b8d06381eb9e4d91dcd02144e7/DropletCollisionImaging (accessed on 13 May 2024).

Conflicts of Interest: The authors declare no conflicts of interest.

Abbreviations

The following abbreviations are used in this manuscript:

AMR	adaptive mesh refinement
CAPES	Coordenação de Aperfeiçoamento de Pessoal de Nível Superior
CICSAM	conservative interpolation convective sharp advection method
CFD	computational fluid dynamics
CFL	Courant–Friedrichs–Lewy
CLSVOF	coupled level-set volume of fluid
FEMEC	Faculdade de Engenharia Mecanica
LIF	laser-induced fluorescent
HRIC	high-resolution interface capturing
PLIC	piecewise linear interface calculation
UFU	Universidade Federal de Uberlandia
VOF	volume of fluid

References

1. Baumgarten, C. *Mixture Formation in Internal Combustion Engines*; Springer Science & Business Media: Berlin/Heidelberg, Germany, 2006.
2. Heywood, J.B. *Internal Combustion Engine Fundamentals*; McGraw-Hill: New York, NY, USA, 1988.
3. Shim, Y.S.; Choi, G.M.; Kim, D.J. Numerical and experimental study on hollow-cone fuel spray of high-pressure swirl injector under high ambient pressure condition. *J. Mech. Sci. Technol.* **2008**, *22*, 320–329. [CrossRef]
4. Li, L.; Green, S.I.; Davy, M.H.; Eadie, D.T. Viscoelastic air-blast sprays in a cross-flow. part 1: Penetration and dispersion. *At. Sprays* **2010**, *20*, 697–720. [CrossRef]
5. Li, L.; Green, S.I.; Davy, M.H.; Eadie, D.T. Viscoelastic air-blast sprays in a cross-flow. part 2: Droplet velocities. *At. Sprays* **2010**, *20*, 721–735. [CrossRef]
6. Fontes, D.H.; Duarte, C.A.R.; de Souza, F.J. Numerical simulation of a water droplet splash: Effects of density interpolation schemes. *Mech. Res. Commun.* **2018**, *90*, 18–25. [CrossRef]
7. Diez, J.; Gratton, R.; Thomas, L.; Marino, B. Laplace pressure driven drop spreading. *Phys. Fluids* **1994**, *6*, 24–33. [CrossRef]
8. de Lima, B.S.; de Souza, Meira, L.; de Souza, F.J. Numerical simulation of a water droplet splash: Comparison between plic and hric schemes for the vof transport equation. *Eur. J. Mech. B/Fluids* **2020**, *84*, 63–70. [CrossRef]
9. Keshavarzi, G.; Yeoh, G.H.; Barber, T. Comparison of the vof and clsvof methods in interface capturing of a rising bubble. *J. Comput. Multiph. Flows* **2013**, *5*, 43–55. [CrossRef]

10. Nikolopoulos, N.; Theodorakakos, A.; Bergeles, G. Normal impingement of a droplet onto a wall film: A numerical investigation. *Int. J. Heat Fluid Flow* **2005**, *26*, 119–132. [CrossRef]
11. Li, R.; Ninokata, H.; Mori, M. A numerical study of impact force caused by liquid droplet impingement onto a rigid wall. *Prog. Nucl. Energy* **2011**, *53*, 881–885. [CrossRef]
12. Malgarinos, I.; Nikolopoulos, N.; Gavaises, M. Coupling a local adaptive grid refinement technique with an interface sharpening scheme for the simulation of two-phase flow and free-surface flows using vof methodology. *J. Comput. Phys.* **2015**, *300*, 732–753. [CrossRef]
13. Malgarinos, I.; Nikolopoulos, N.; Marengo, M.; Antonini, C.; Gavaises, M. Vof simulations of the contact angle dynamics during the drop spreading: Standard models and a new wetting force model. *Adv. Colloid Interface Sci.* **2014**, *212*, 1–20. [CrossRef] [PubMed]
14. Yu, X.; Shang, B.; Xie, B.; Huang, M.; Luo, X. Spreading behaviors of silicone droplet impact on flat solid surface: Experiments and vof simulations. In Proceedings of the 2015 16th International Conference on Electronic Packaging Technology (ICEPT), Changsha, China, 11–14 August 2015; IEEE: Piscataway, NJ, USA, 2015; pp. 1058–1061.
15. Chen, B.; Li, J.; Mao, F.; Tian, R. Numerical study on the characteristics of single wetted flat wire with single droplet impact under the disturbance of airflow. *Nucl. Eng. Des.* **2019**, *345*, 74–84. [CrossRef]
16. Xiao, D.; Li, X.; Hung, D.L.; Xu, M. *Characteristics of Impinging Spray and Corresponding Fuel Film under Different Injection and Ambient Pressure*; Technical Report; SAE International: Warrendale, PA, USA, 2019.
17. Zhao, L.; Ahuja, N.; Zhu, X.; Zhao, Z.; Lee, S.Y. *Splashing Criterion and Topological Features of a Single Droplet Impinging on the Flat Plate*; Technical Report; SAE International: Warrendale, PA, USA, 2018.
18. Mawarsih, E.; Budiana, E.P.; Deendarlianto, Indarto, Kamal, S. Numerical simulation of single droplet phenomenon using method finite difference and front-tracking. In *AIP Conference Proceedings*; AIP Publishing LLC: Melville, NY, USA, 2020; p. 020016.
19. de Lima, B.S. Dropletcollisionimaging. 2022. Available online: https://github.com/brunosdlima/CFD/tree/main/DropletCollisionImaging (accessed on 13 May 2024).
20. Richards, K.; Senecal, P.K.; Pomraning, E. *Converge v2.3 Manual*; Convergent Science, Inc.: Madison, WI, USA, 2016.
21. Brackbill, J.U.; Kothe, D.B.; Zemach, C. A continuum method for modeling surface tension. *J. Comput. Phys.* **1992**, *100*, 335–354. [CrossRef]
22. Samenfink, W.; Elsäßer, A.; Dullenkopf, K.; Wittig, S. Droplet interaction with shear-driven liquid films: Analysis of deposition and secondary droplet characteristics. *Int. J. Heat Fluid Flow* **1999**, *20*, 462–469. [CrossRef]
23. Stalder, A.; Kulik, G.; Sage, D.; Barbieri, L.; Hoffmann, P. A snake-based approach to accurate determination of both contact points and contact angles. *Colloids Surfaces A* **2006**, *286*, 92–103. [CrossRef]